Study of the Pressure Distribution on an Aircraft Tire-Wheel Interface

James A. Sherwood*
University of Massachusetts-Lowell, Lowell, Massachusetts 01854
and
Barry K. Fussell,† William R. Edwards,‡ Todd S. Gross,† and David W. Watt†
University of New Hampshire, Durham, New Hampshire 03824

The pressure distribution at the tire-wheel interface is not presently well understood, despite the need for using this load distribution to design fail-safe wheels. To investigate this boundary condition, methodologies for accurately measuring the distribution were investigated using an F-16 main wheel subjected to the inflation-pressure condition. A purely experimental approach using piezoelectric film measured the interface pressure at eight discrete points in the tubewell, beadseat, and flange regions of the wheel. A hybrid technique used the experimental method of holographic interferometry to measure the wheel displacements and a three-dimensional finite element method was used to backcalculate the pressure distribution based on these experimental displacements. A comparison of the two methodologies is given. Areas of high stress are determined and discussed with respect to ensuring a fail-safe design.

I. Introduction

A IRCRAFT wheels are designed to exhibit a fail-safe point so that a crack in the wheel can be detected before any catastrophic failure occurs. This fail-safe point is typically where the tubewell meets the web of the wheel. This fail-safe point as well as other major regions of an aircraft wheel are depicted in Fig. 1. The concept is to have this fail-safe point demonstrate a lower fatigue life than any other area of the wheel. Thus, a fatigue crack will initiate in this area, result in a leak, and ultimately a flat tire, i.e., leak before burst. This flat tire can be detected on the flight line during a standard preflight inspection.

Aircraft wheels also potentially have a fatigue critical area where the tire contacts the rim, also known as the flange and beadseat regions. If either one of these regions is more critical than the fail-safe region, then fatigue-crack growth in this tire-contact region can lead to catastrophic failure, i.e., burst before leak. This undesirable condition is a consequence of the tire seating against the rim, thereby prohibiting the crack from leaking. Hence, the crack can become critical before ever being detected. The wheel-design engineer's task is therefore a compromise of making the fail-safe region more fatigue critical than the contact region while maintaining a design of minimal weight and guaranteed roll life.

Currently, wheel design is heavily dependent on experimental strain-gauge investigations of the structural response of the wheel. This experimental process is time-consuming. If the load distribution at the tire-wheel interface were known, then analytical methods such as finite element methods could be used to expedite the design process. The U.S. Air Force recognizes this need and has supported efforts to achieve this goal of analytical investigations.[1-3]

The load distribution at the tire-wheel interface is very complicated in nature, and a definitive work concerning this load region has not been available in the past. The complexity is a consequence of the nonlinearity of the tire-wheel combination. The tire and the wheel each exhibit very dissimilar deformation characteristics. The wheel is composed essentially of an isotropic, homogeneous, linear-elastic material undergoing small deformations. In contrast, anisotropic, inhomogeneous, nonlinear materials exhibiting relatively large deformations constitute the tire. An additional complexity is introduced by the size of the tire-wheel contact area being a function of the loading condition under consideration.

Various attempts have been performed by others to experimentally investigate the distribution of the loads at the tire-wheel interface. One of the earliest reports discussing the experimental investigation of the normal contact pressure at the tire-rim interface was published by Zaharov.[4] Pressure values were recorded by strain gauges mounted on a cantilevered beam built into a special housing. This housing was welded to a 40.64-cm- (16-in.-) diam wheel. Balabin and
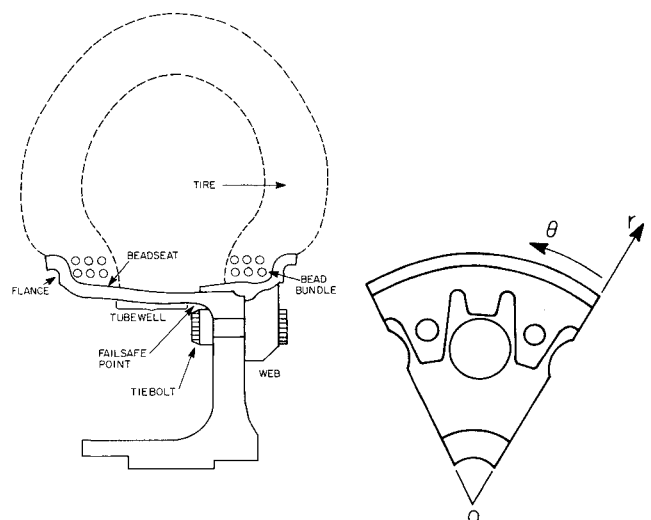
*Associate Professor, Department of Mechanical Engineering, One University Avenue. Member AIAA.
†Associate Professor, Department of Mechanical Engineering.
‡Graduate Student, Department of Mechanical Engineering.

Fig. 1 Overall wheel geometry and cylindrical reference frame.

Zubarev[5] made extensive measurements of the bead contact pressure on wide base truck tires mounted on 50.8-cm- (20-in.-) diam wheels for a variety of rim widths. Normal pressures were recorded at 16 locations in the flange/beadseat region of the wheel for loads due to inflation and rolling. A more recent experimental evaluation of the normal forces imposed upon the wheel by tire contact was conducted by Walter and Kiminecz.[6] Normal forces were measured using a miniature magnetostrictive transducer, 0.127 cm (0.050 in.) in diameter, as the load sensor. To mount the transducer to the wheel, the transducer was embedded in a bolt and encapsulated in a polyurethane potting compound. The transducer-bolt assembly was then fit into a drilled and tapped hole in the rim. In all of these experimental investigations, only the normal forces were directly measured. Hence, the value of the shear forces remains unknown due to the lack of instrumentation for the measurement of these tractions. In addition, these methods were intrusive to the wheel rim. The welding and drilling operations used to mount the measuring devices change the structural characteristics of the wheel. Thus, the techniques used to measure these loadings are potentially changing the real loading situation. Chen[7] completed a two-dimensional finite element study of a wheel–tire model. His study modeled the tire and assumed the wheel to be rigid.

The goal of the present study was to investigate, design, and verify the applicability of methodologies for measuring the tire–wheel interface loads that were nonintrusive and considered the deflection of the wheel. In this study, only the boundary conditions associated with the static loading of the tire–wheel assembly due to inflation pressure were investigated. A purely experimental technique using piezoelectric film was employed to measure the distribution directly, and a hybrid experimental–analytical effort involving holographic interferometry and a three-dimensional finite element model was used to backcalculate interface loads. All investigations were completed using an F-16 main wheel.

II. Methods

A. Piezoelectric Film

Piezoelectric film was selected as a possible candidate for this measurement application. This selection was based on piezoelectric film being very flexible and thin (52 μm). These two characteristics allow for minimal intrusion in the contact area.

To get the pressure distribution along the beadseat, the film samples were incremented radially outward at several circumferential locations around the wheel. To document the credibility of this experimental method, one gauge was mounted away from the tire in the tubewell. An all-purpose ethyl cyanoacrylate was used to bond the gauges to the rim. To protect the instrumentation from the shear forces encountered during assembly and inflation–deflation of the wheel, Teflon® strips were placed over the gauges and along the lead wires. The Teflon strips also acted as insulation between the gauge terminals and the wheel rim. Eight gauges were mounted on the rim as shown in Fig. 2. These locations were selected to coincide with nodes of the finite element model used in the analytical portion of the study. Table 1 summarizes these locations and Fig. 1 denotes the reference frame on the wheel.

Piezoelectric film is a dynamic device, and its piezoelectric property is a function of its crystalline structure. The films are used extensively for measuring pressure distributions.[8] The film selected for this study is polyvinylidene fluoride (PVDF), which is a long-chain semicrystalline polymer of the repeat unit (CH_2—CF_2). Units of the monomer, vinylidene fluoride CH_2=CF_2, polymerize in an orderly fashion to give greater than 90% head-to-tail configuration: —CH_2—CF_2—CH_2—CF_2—. This ordered structure also gives rise to an anisotropic response. When the film is deformed,

Table 1 Locations of piezoelectric film on inboard half of rim

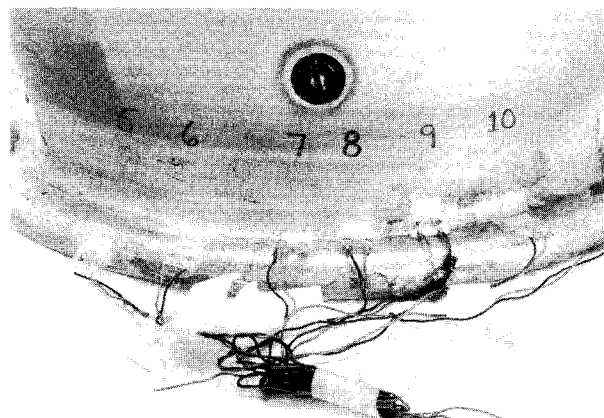| Inboard gauge number	Radius, cm	θ, deg	Z, cm
1	16.76	19	7.14
3	17.27	0	4.29
4	18.54	4	1.91
5	19.81	1	1.27
6	18.54	12	1.91
7	18.03	36	1.91
8	17.78	26	2.24
9	17.53	17	2.84

Fig. 2 Piezoelectric gauge locations.

it exhibits an instantaneous voltage change that decays over a short period as a result of leakage resistance. By adding a charge amplifier to each film gauge, the time constant of the decay can be increased sufficiently ($\tau = 200$ s) to allow quasistatic measurements. However, since inflating the tire from zero to rated pressure requires several minutes, the piezoelectric film measurements have to be taken at discrete pressure increments to avoid the loss of steady-state data. To find the wheel–tire pressure indicated by the film gauge at a particular inflation pressure, all the incremental gauge readings taken up to the given inflation pressure are summed. For each reading, the film gauges were first zeroed, the inflation pressure was incremented 70 kPa (10 psi), and the voltage change recorded using LabTech Notebook® software on an IBM AT compatible personal computer. The tire was seated properly such that no leaking occurred by inflating to 1900 kPa (275 psi) and releasing the pressure back down to 170 kPa (25 psi).

For this study, the film deformed as a result of the tire contact loads and the in-plane straining of the wheel. To use the device to measure only the contact pressure, the in-plane strain contribution to the voltage change had to be subtracted from the total response. To quantify the effect of in-plane strain on the gauge output, a piezoelectric-film gauge was mounted adjacent to a strain gauge on a cantilevered aluminum beam. The beam was subjected to a strain field by suspending weights from the free end of the beam, and the corresponding strain-gauge and piezoelectric-film responses were recorded. The results are given in Fig. 3. This figure shows that the in-plane strains do indeed induce a voltage change in the film in the absence of any normal pressure. Therefore, the voltage values accumulated by summing the incremental voltages during the inflation of the tire needed to be corrected by subtracting the influence of the in-plane strains of the wheel at the respective location of each gauge for tensile strain, and adding the influence for compressive strains.
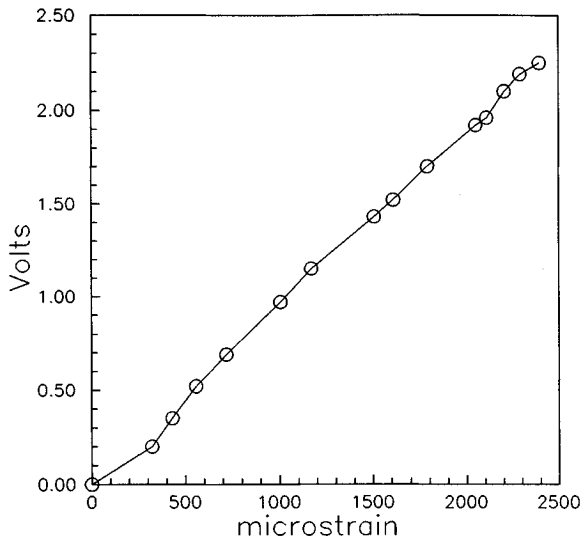
Fig. 3 Piezoelectric film response to in-plane strain.

B. Holographic Interferometry

Holographic interferometry was used as a measurement method to provide a map of the out-of-plane displacements on the inboard and outboard halves of the wheel during inflation. These displacements are the direct result of the applied forces of the tire on the wheel due to inflation. The accuracy of this method as used in this study is 0.15 μm.

The electro-optic holographic interferometry system used for this effort is described in more detail in Gross et al.[9] and Raber.[10] Briefly, a laser beam is split into two equal paths by coupling into a pair of optical fibers. One path, the reference beam, is directed to impinge on the detector in a charge-coupled device (CCD) solid-state camera through an 80-20 beam splitter. The other path, the object beam, is directed perpendicularly to the object through a 50-50 beam splitter and imaged through a camera lens onto the detector. Since these two beams are coherent, they will interfere. The spatial variation of phase difference between the object and reference beam is determined by recording four consecutive images in which the path length of the reference beam is shortened by $\lambda/4$ between each successive image, where λ is the wavelength. The phase ϕ is calculated on a pixel-by-pixel basis, according to the expression

$$\phi(x, y) = \tan^{-1}\left[\frac{I_4(x, y) - I_2(x, y)}{I_1(x, y) - I_3(x, y)}\right] \qquad (1)$$

where I_i is the intensity at each pixel for the ith exposure.

As the object is deformed, the path length between the object and the detector varies resulting in a change of phase at the detector. The phase map is recalculated for the deformed object, and the two maps are subtracted from one another. The phase difference $\Delta\phi$ is proportional to the displacement Δz of the object according to the expression

$$\Delta z = (\lambda/4\pi)\Delta\phi \qquad (2)$$

for normal illumination and viewing. The map of the phase difference encodes the phase modulo 2π.

Normally, the phase is automatically unwrapped using an error tolerant algorithm.[11] However, for the present study the fringe density was too great for this approach, and the fringe order was manually entered at each point corresponding to a node in the finite element model. In addition, as can be seen in Fig. 4, the fringes were not continuous in certain areas of the interferogram, resulting in an uncertainty in the fringe order. The effect of this uncertainty is discussed later. The
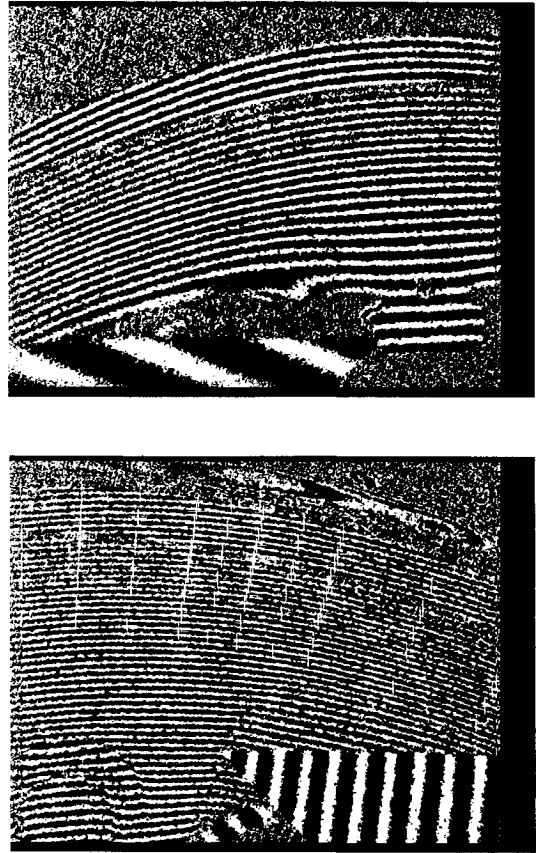

Fig. 4 Interferograms of the inboard and outboard halves.

fringe orders were counted relative to a fixed point on the optical table. The displacements were measured at several discrete pressures. A semilinear regression scheme, which is discussed later, was used to accumulate the deflections over the entire inflation pressure range.

C. Finite Element

The F-16 main wheel exhibits essentially 10 planes of circular symmetry, and the inflation-pressure-load condition under consideration in this study is axisymmetric. Therefore, by taking advantage of these symmetry situations, only a 36-deg wedge of the wheel was modeled for the analytical portion of the investigation. The wheel was constructed using 20-noded isoparametric bricks, and the integration order was $3\times3\times3$. The wheel material is 2024-T6 aluminum with an elastic modulus of 69 GPa (10×10^6 psi) and Poisson ratio of 0.3. The load distribution due to the tire acting on the wheel was applied by using the displacements as measured during the holographic interferometry. Thus, the tire is not modeled explicitly in this study. All the finite element analyses were completed using Version 5.6 of the commercially available program ADINA by ADINA R&D, Inc. of Watertown, Massachusetts.[12] All phases of the finite element work, i.e., preprocessing, finite element analysis, and postprocessing, were completed on an IBM RS/6000 Model 530 workstation.

To simulate the bolt preload in the tie-bolt, an induced-thermal-strain modeling technique was implemented by cooling the shank of the bolt. This cooling results in a contraction of the bolt shank and pulls the two wheel halves together. The bolt shank was cooled until a tensile stress of 6900 MPa (100 ksi) was developed in the shank of the bolt. This value of 6900 MPa (100 ksi) is the standard prescribed bolt preload for aircraft wheels.

To decrease the magnitude of erroneous radial shear forces in the bolt, the bolt head and sleeve were connected to the

bolt shank using multipoint constraints (MPCs). This modeling approach eliminated the need to use the contact option between the head and the wheel. The MPC option prescribed that the coincident nodes at the wheel-bolt head interface and the coincident nodes at the shank-bolt head interface displace the same amount in the axial direction. This MPC modeling technique permits the radial movement of the shank nodes and the radial movement of the head and sleeve nodes to be independent. This independence prohibits the buildup of any artificial radial tractions between the bolt head and wheel during the creation of the preload using thermal strains since only the nodes on the shank experience the temperature change ΔT. Hence, the bolt head nodes see no ΔT and experience no radial contraction. Otherwise, the bolt heads would move radially during the cooling process and this radial motion would in turn cause radially directed friction forces. This scheme demonstrated the added benefit of requiring less CPU time to develop the proper preload in the bolt than would be necessary had the contact-surface option been used in this area of the model.

The holographic displacement data were used to apply displacement loads on the wheel rim. Only displacements in the axial direction of the wheel were applied in the finite element portion of the investigation. For this study, it was assumed that the axial displacements were the dominant displacements for the inflation pressure condition, as they are normal to the flange. Any radial or circumferential displacements were assumed to have an insignificant effect on the flange forces. The loading of the wheel in ADINA was accomplished in six time steps. The first three time steps were used to generate the bolt preload of 6900 MPa (100 ksi). The three steps were necessary as a consequence of the nonlinearity of the solution due to the presence of the contact surfaces between the wheel halves. The fourth, fifth, and sixth time steps were used to impose displacements corresponding to 483, 1172, and 1862 kPa (70, 170, and 270 psi), respectively. The ADINA program calculated the nodal forces required to achieve these displacements. These nodal forces were then translated into effective pressures on the elements comprising the tire-contact region.

III. Results

A. Piezoelectric Film Results

Table 2 is a summary of the voltage corrections for the in-plane strain contribution to the total loading voltage. The in-plane strains were extracted from the results of the finite element analysis where the wheel model was loaded with the displacements as measured by the holographic interferometry. The total voltage values were adjusted by these corrections to obtain the normal pressure without the extraneous effect of in-plane straining. Figure 5 depicts the pressure distribution on the inboard half of the rim at the maximum inflation pressure of 1862 kPa (270 psi). A peak value of 4854 kPa (704 psi) was obtained at gauge 7, which is on the flange. Pressure values for gauges under the tire decreased above and below the radial location of this gauge. Gauge 3 exhibited a zero
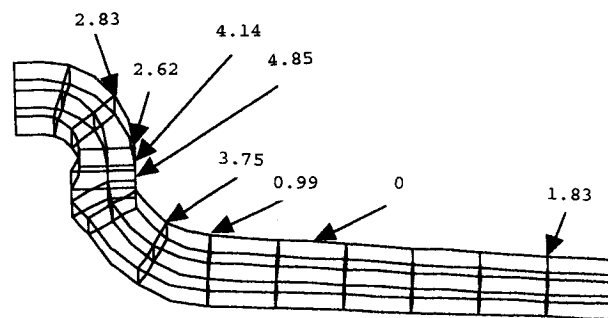

Fig. 5 Finalized pressure distribution on the inboard half flange of rim in MPa.

pressure. This value may appear unusual, but is not surprising. The entire foot of the tire is not necessarily in intimate contact with the wheel for all loading conditions. Thus, this zero value reflects the lack of tire contact at this point for this loading condition, i.e., essentially a small void between the tire and the wheel. The gauge in the tubewell, i.e., not in contact with the tire, exhibited a value of 1827 kPa (265 psi). This value is within 2% of the 1862-kPa (270-psi) inflation pressure and provides credibility for the method to measure contact pressure. It can also be seen in this figure that the magnitude of the pressure in the beadseat is indeed less than the pressure on the flange. This result is physically reasonable as it is assumed that the tire seats more completely against the flange than it does in the beadseat radius.

B. Holographic-Interferometry Results

The holographic displacement data were relative to an initial zero displacement. The experimental data were available for deflections at pressures of 1655, 1724, and 1793 kPa (240, 250, and 260 psi), relative to a zero displacement at 1862 kPa (270 psi); 965, 1034, and 1103 kPa (140, 150, and 160 psi), relative to a zero displacement at 1172 kPa (170 psi); and 276, 345, and 414 kPa (40, 50, and 60 psi), relative to a zero displacement at 483 kPa (70 psi). To accumulate these relative displacements into a total absolute displacement, the data needed to be processed. The processing involved the integration technique where the incremental values were accumulated.

The overall displacements are a nonlinear function of pressure. However, to translate the data into a useful form, the displacement as a function of pressure was assumed to be essentially linear over a 207-kPa (30-psi) differential, i.e., 1862–1655 kPa (270–240 psi), 1172–965 kPa (170–140 psi), 483–276 kPa (70–40 psi). This assumed form allowed for a linear regression of the displacements as a function of inflation pressure for the data at 1655, 1724, and 1793 kPa (240, 250, and 260 psi). From this regression, the slope was obtained. This straight line fit was forced to have zero displacement at 1862 kPa (270 psi), the starting pressure for the experimental observations. The slope was assumed to be constant between 1379–1862 kPa (200–270 psi). Next, a linear regression was performed for the 965-, 1034-, and 1103-kPa (140-, 150-, and 160-psi) data. This straight line fit was assumed to be constant between 690–1379 kPa (100–200 psi) and was forced to intersect the 1379- to 1862-kPa (200- to 270-psi) fit at 1379 kPa (200 psi). Finally, the linear regression and shifting scheme was repeated for the 276-, 345-, and 414-kPa (40-, 50-, and 60-psi) data. This line was forced to intersect the 690- to 1379-kPa (100- to 200-psi) line at 690 kPa (100 psi), and was assumed to have a constant slope from 0 to 690 kPa (100 psi). Figure 4 shows typical interferograms for the inboard and outboard halves, respectively.

The raw data and the processed data for a typical outboard-wheel-half node are shown in Fig. 6. This figure shows that the deflection increases with increasing pressure as expected.

Table 2 Voltage change in piezoelectric film as a function of in-plane strain

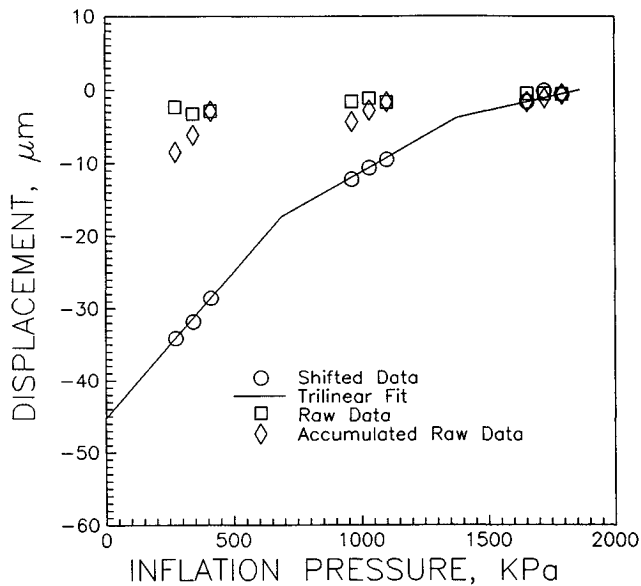| Inboard gauge number	In-plane strain, $\mu\varepsilon$	Voltage change due to in-plane strain, V
1	660	0.57
3	1425	1.00
4	468	0.40
5	−715	−0.95
6	844	0.80
7	680	0.63
8	2310	2.20
9	2021	1.90

Fig. 6 Raw and processed holographic data for a typical nodal location.

The data also shows that the magnitude of the deflection increment is indeed a nonlinear function of the pressure. The increment of deflection per increment of pressure decreases with increasing pressure. This nonlinearity is reasonable and can be explained by the stiffening of the tire. As the inflation pressure increases, the effective elastic modulus of the tire increases. The elastic modulus of the aluminum wheel is constant. Therefore, by the rule of mixtures, for each increment in inflation pressure, a greater fraction of the total load is assumed by the tire. Consequently, the aluminum wheel's fraction of the total load drops as the inflation pressure increases. Thus, since the wheel stiffness is constant, the wheel deflections are linearly proportional to the forces acting on it. This phenomenon has been observed by engineers at B.F. Goodrich. However, the experimental method used by these engineers only gave insight as to the total force on the flanges. Using displacement loads in the finite element method has the potential of yielding the total force as well as the variation of this force along the wheel.

C. Finite Element Results

The finite element plots presented are at the maximum pressure condition. Figure 7 represents a complete 36-deg wedge of the finite element model of an F-16 main wheel. The geometries of both the inboard and outboard halves can be identified, as well as the tie bolt head. In all of the plots comparing the original shape of the wheel to the deformed geometry, the deformations of the wheel are greatly exaggerated for visualization purposes. In all the plots comparing the deformed shape to the undeformed shape, the deformed shape is represented by solid lines, and the original shape is given by the dashed lines.

Figure 8 is a side view of a one-element-wide slice of the model of the F-16 wheel at the 1862-kPa (270-psi) loading. This slice corresponds to a single radial line of brick elements and is essentially a 4-deg arc. As was prescribed by the displacement loads, the flanges move outward. As a consequence of these imposed displacements, the tubewell, beadseat, and flange of the inboard half move axially out and radially in. The outboard half of the wheel is very stiff and essentially displaces by pivoting about the tie bolt with little deformation.

It can be seen in Fig. 8 that basically all the deformation in the assembled wheel occurs outside the tie-bolt circle. The stretching and bending deformations of the tie bolt are physically in the proper directions. The overall displacement is
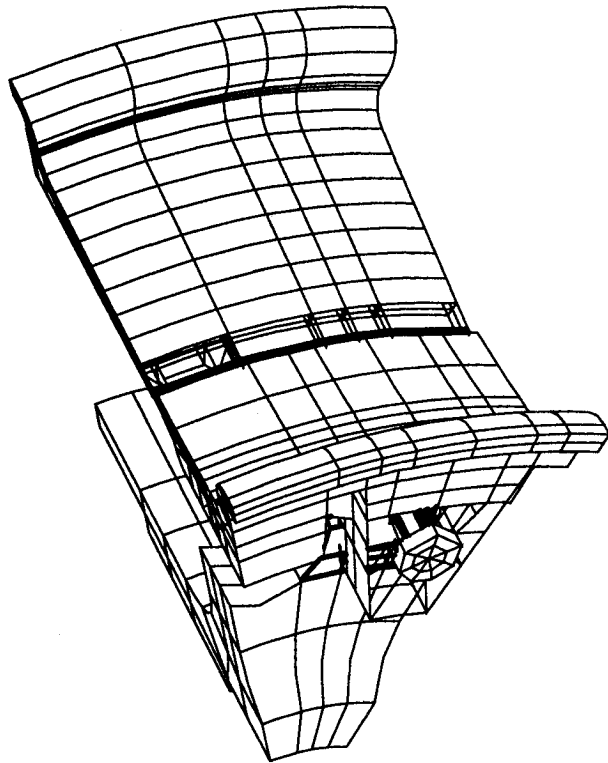

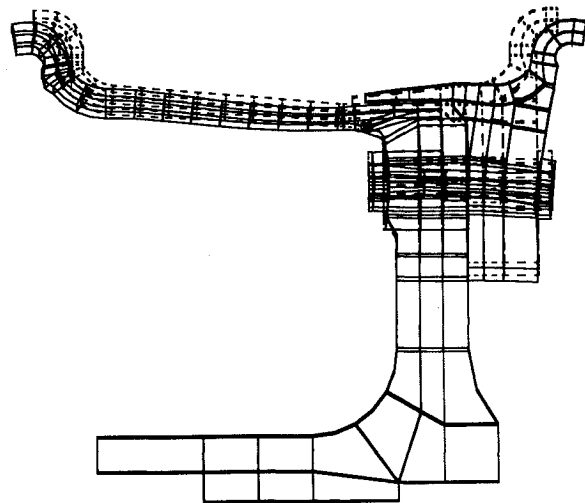Fig. 7 Complete view of wheel with hidden lines removed.

Fig. 8 Side view of a one-element-wide slice of the F-16 model at 1862 kPa.

reasonable since all the loading is in the outer region of the tire–wheel assembly. The portion of the wheel from the tie-bolt circle inward to the axle is essentially load free. This 36-deg wedge of the model also makes it possible to notice the minimum axial displacement at the circumferential location of the drive lug.

Figure 9 is a contour plot of the effective stress σ_{EFF} of the inboard half of the wheel at 1862 kPa (270 psi). The effective stress is the standard von Mises form and is written as

$$\sigma_{EFF} = [\tfrac{1}{2}\{(\sigma_x - \sigma_y)^2 + (\sigma_y - \sigma_z)^2 + (\sigma_z - \sigma_x)^2\} + 3(\tau_{xy}^2 + \tau_{yz}^2 + \tau_{zx}^2)]^{1/2} \qquad (3)$$

As depicted in this figure, areas of relatively high stress can be observed in the heel of the beadseat (point A) and in the
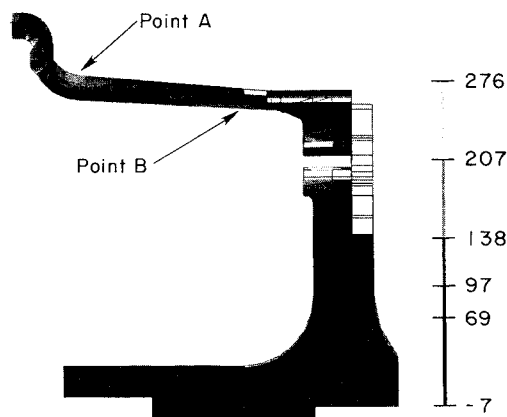
Fig. 9   Contour plot of the effective stress (MPa) in the inboard half of the wheel at 1862 kPa.

fail-safe location (point B). These are the two high-stress areas of interest. High stress due to the bolt loading, represented in the web region of the rim, can also be noticed. The load condition under consideration only corresponds to that of rated inflation. No conclusion should be made that this wheel is not a fail-safe design just because the effective stress at point A is greater than the effective stress at point B. Field service conditions may prove that point B is overall more critical than point A.

The highest stress in the beadseat region is in the 160-MPa (23-ksi) range, whereas in the fail-safe location the highest stress is in the 110-MPa (16-ksi) range. These are effective stress values before the superposition of any mechanical working to induce compressive stresses on the surface. Stress rolling in the beadseat and shot peening in the fail-safe region are two surface treatments used on aircraft wheels. These surface treatments, which are a standard operation of the manufacturing process, act to reduce the magnitude of the tensile working stresses and are not superimposed on these plots. The highest-stress location on the outboard (OB) half is at the tangent point of the beadseat radius and is approximately 83 MPa (12 ksi).

Figure 10 is a top view of the wheel. In this figure, it can be seen that the inboard beadseat stress varies in intensity as a function of the circumferential location. This variation can be attributed to the influence of material-thickness variation in different sections of the wheel. The drive lug is located at the top part of this figure. This additional material has a significant influence on the stress distribution. The outboard half of the wheel [on the left-hand side (LHS) of the picture] exhibits an overall lower stress field as compared to the inboard half. Further inspection of a hub view of the inboard half of the wheel shows that the stress in the fail-safe region also varies as a function of circumferential location. This variation is shown in Fig. 11. This variation in stress is again attributed to the presence of the drive lug in the upper portion of the figure. The high stress located in the lower right of the picture is due to the tie bolt.

The resultant flange forces are summarized in Table 3 for 483-, 1172-, and 1862-kPa (70-, 170-, and 270-psi) inflation pressures. The resultant inboard forces translate to average pressures of 6033, 9725, and 12,048 kPa (875, 1410, and 1747 psi), respectively, acting on the flange with an area of 30.32 cm² (4.7 in.²). These inboard pressure values are 12.5, 8.3, and 6.5 times the inflation pressures of 483, 1172, and 1862 kPa (70, 170, and 270 psi), respectively. The resultant outboard forces translate to average pressures of 5568, 9011, and 11,323 kPa (807, 1306, and 1642 psi), respectively, acting on the flange. These pressure values are 11.5, 7.7, and 6.1 times the inflation pressure. These effective pressure values are using a 36-deg arc with a 2.54-cm (1-in.) flange, which has a 35.56-cm (14-in.) i.d.

Table 3   Total forces and average pressures in the flange region of the wheel at three different inflation pressures

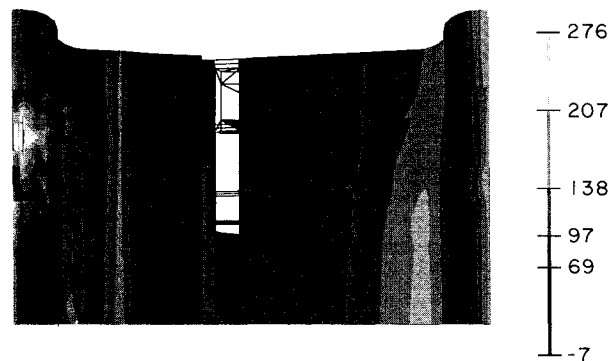| Inflation pressure, kPa	Inboard reaction, N	Outboard reaction, N	Average inboard pressure, kPa	Average outboard pressure, kPa
483	−17,721	16,355	6,033	5,568
1,172	−28,565	26,466	9,725	9,011
1,862	−35,388	33,258	12,048	11,323

Fig. 10   Top view of the F-16 wheel model effective stress (MPa) contours.
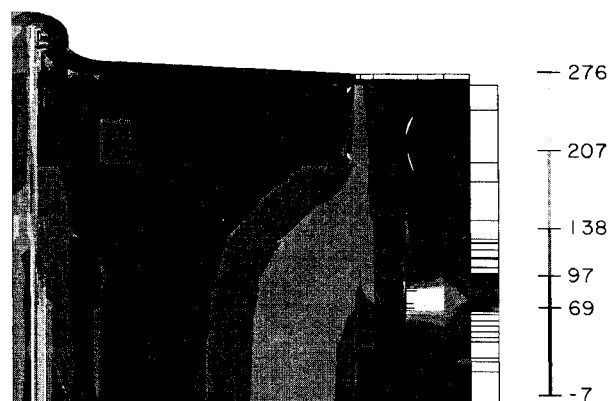

Fig. 11   Hub view of inboard wheel half identifying circumferential distribution of fail-safe effective stress (MPa).

The respective backcalculated inboard and outboard average flange pressures (forces) are essentially within 8% of one another for all time steps of the loading. Theoretically, these forces should be equal in magnitude and opposite in direction. Any deviation in magnitude equality is most likely due to the experimental procedure of recording the inboard and outboard deflections in independent tests. However, taking this experimental procedure into consideration, an 8% difference is understandable and within reason.

To backcalculate the pressure distribution on the finite element model, a weighted load displacement technique was used. This technique involved reloading the wheel with displacements as prescribed on the beadseat region of the wheel from the holographic loading, while turning off the holographic displacement loading on the outer side of the flange. Thus, the displacements were prescribed where the tire was potentially in contact with the wheel. The remainder of the wheel tubewell was subjected to a pressure loading equal to the inflation pressure. The results of the finite element analysis include the reaction forces at the prescribed displacement locations. The resultant force at a given node is the superposition of the contributions of the consistent load vector for

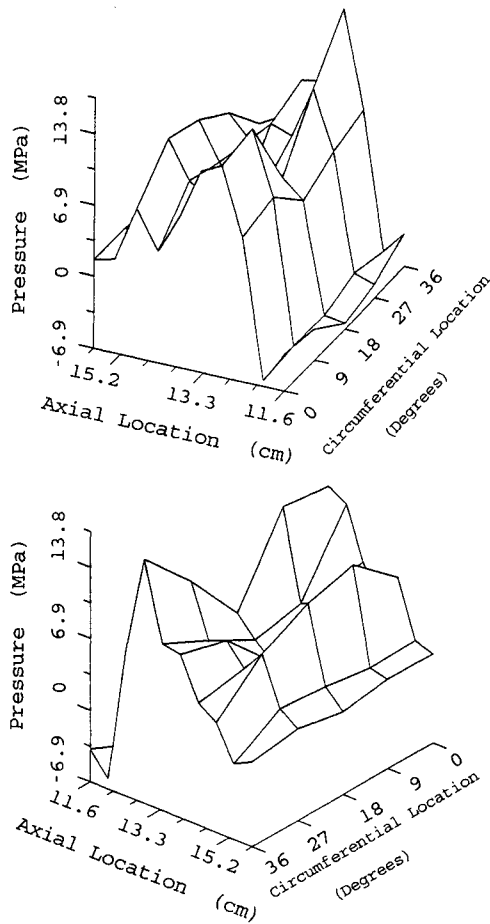Fig. 13 Map comparing finite element and piezoelectric pressures in MPa.

Fig. 12 Backcalculated pressure distribution from the finite element model.

each element connected to this node. A consistent load vector is the set of discrete nodal forces that correspond to a given pressure distribution on the element. Only the elements connected to a node can contribute to its resultant force. For the present study, the pressure distribution was assumed to be uniform across each element. Each element's weighted contribution to the resultant nodal force was assumed to be the product of the element's area A, the normal pressure acting on the element P, and the respective consistent load vector factor for that node, F. The value of A can be found by computing the surface area. For a 20-noded brick, the value of F is known to be $-P^*A/3$ for a corner node and $P^*A/12$ for a midside node. Considering all the nodes and elements associated with the tire-contact region, a complete and nontrivial set of linear simultaneous equations is developed where the unknowns are the pressure values for each of the elements in that region. Use of this technique allowed for a pressure distribution corresponding to the displacement loading in the beadseat to be easily backcalculated. Two views of the distribution are shown in Fig. 12. While these surface plots are difficult to interpret, they do show the circumferential and radial pressure variations. Peak pressure values are noticed for the flange region. This peak pressure region corresponds to that which was determined using the piezoelectric film as given in Fig. 6.

IV. Comparison of Piezoelectric and Finite Element Pressure Distributions

Figure 6 summarizes the pressure values for the maximum inflation pressure as measured by the piezoelectric film, and Table 3 summarizes the EOHI-FE results. In comparing the average pressure on the tire-wheel contact surface as deter-
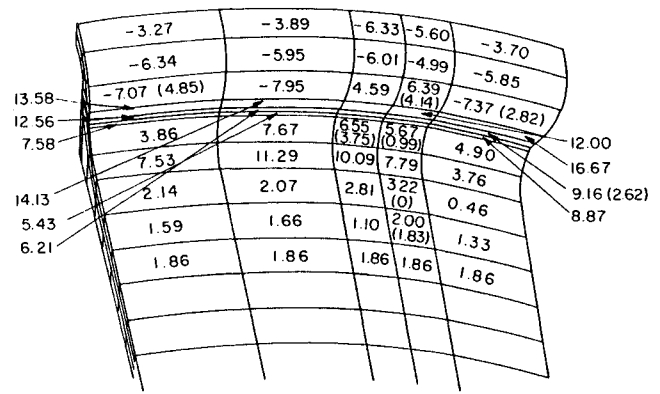
mined by the finite element method to the pressures measured by the piezoelectric method, it can be seen that the average finite element pressure is greater than any of the piezoelectric values. This is a disturbing result since the piezoelectric method is credible because it was able to capture the inflation pressure within 2%. Figure 13 is a crude map of the contact pressures backcalculated from the holographic data for each of the elements in the finite element model. The piezoelectric pressures are included in parentheses. As can be seen in this figure as well as was seen in Fig. 12, the finite element pressure distribution varies significantly over the contact surface. This "piecewise continuous" distribution demonstrates many peaks and valleys. Thus, it is feasible that the piezoelectric measurements were not at peak-pressure locations. A close examination of Fig. 13 shows that the variation of the piezoelectric pressures parallels the variation of the finite results. Thus, while the two methods do not yield the same magnitudes of pressure for a given location, the overall pressure variations show the same trends.

The presence of the negative values on the pressure map are unrealistic since the tire cannot pull on the wheel. However, their presence may explain why the difference in the pressure values between the two methods was so great. For the finite element investigation, it was assumed that the axial displacements were the critical displacement component. The radial displacements were not prescribed in the analysis. Hence, what radial displacements did occur in the analysis were a direct consequence of the applied pressure in the portion of the tubewell that was not in contact with tire and of the prescribed axial displacements in the contact area. Thus, to achieve the prescribed axial displacements in the absence of prescribed radial displacements, a net force larger than reality was required in some portions of the contact region and negative pressures were required in other areas. Thus, it is concluded that the radial displacements may be critical inputs to the finite element analysis for backcalculating the pressure distribution.

Another source of error in the hybrid method may be the limited number of pressures investigated. The scheme used to accumulate the holographic data into a total displacement over the entire inflation-pressure range assumed the relation to be trilinear. In reality, the slope of this relation is constantly decreasing with increasing pressure. By assuming this slope to be constant over wide pressure increments, the accumulated displacements were larger than the actual displacements. These "too large" displacements backcalculate to "too high" pressures.

V. Conclusions

Two methods were investigated for noninvasively investigating the pressure distribution at the tire-wheel interface. The piezoelectric method proved credible as it was able to

correctly capture the known inflation-pressure value. However, the piezoelectric method requires knowing the in-plane strain field at the gauge location to isolate the voltage change due to pressure. The hybrid method involved using the finite element technique to backcalculate the load distribution from the holographic interferometry data. The piezoelectric film only captured the pressure at discrete points, while the hybrid method produced a piecewise continuous pressure-distribution picture.

Both methods showed the same trends in pressure variation for the contact region. However, the hybrid method exhibited higher pressure values than did the film at the same location. In addition, the hybrid method produced unrealistic negative pressures on the top of the flange. The difference between the pressure values for the two methods is attributed to two possible sources. One source is the assumption that only the axial components of displacement were critical inputs to the finite element technique. Accuracy could possibly be improved with the inclusion of radial displacements. Another source of error was the limited number of inflation pressures for which displacement data were available. This limited data resulted in accumulated displacements which were too large.

Presently, no known instrumentation techniques exist that allow for the determination of the shear forces at the tire–wheel interface. However, the hybrid method could provide a technique for determining the shear force distribution in the beadseat area. Using the displacement data in the finite element model, a parametric study could be completed to determine the appropriate value of the coefficient of friction μ between the wheel and the tire and shed insight into the magnitude of the shear forces. With additional insight into this traction distribution at the interface, wheel designers will be better able to migrate from a time-consuming, experimentally driven design process to a more cost-effective analytically driven one. The use of holographic interferometry can be used to calibrate the finite element method. The ultimate goal is to have a good understanding of the pressure distribution at the interface such that the finite element method can be used with confidence in the absence of experimental data. This study has initiated that goal.

Acknowledgments

References

[1]Brockman, R. A., Braisted, R. A., Padovon, J., Tabador, F., and Clark, S., "Design and Analysis of Aircraft Tires," Univ. of Dayton Research Inst., UDR-TR-89-14, Dayton, OH, Feb. 1989.

[2]Treanor, D. H., and Carter, T. J., "Military Aircraft Wheel Life Improvement Assessment," AFWAL-TM-88-152, Wright–Patterson AFB, OH, 1987.

[3]Sherwood, J. A., and Holmes, N. C., "Development of an Aircraft Tire-Wheel Interface Model for Flange/Beadseat Contact Loads," 1988 USAF-UES Summer Faculty Research Program/Graduate Student Program, 1988.

[4]Zaharov, S. P., "Feasibility Study of How to Make Compression Measurements of the Tire Bead Against the Rim," *Kauchuk I Rezina*, Vol. 16, No. 8, 1957, pp. 30, 31 (in Russian).

[5]Balabin, I. V., and Zubarev, N. A., "Force Interaction Between a Wide Profile Tire and the Wheel Rim," *Automobil'naya Promyshlennost*, Vol. 30, No. 6, 1964, pp. 16–19 (in Russian).

[6]Walter, J. D., and Kiminecz, R. K., "Bead Contact Pressure Measurements at the Tire-Rim Interface," *Automotive Engineering Congress and Exposition*, Society of Automotive Engineers Paper 750854, Detroit, MI, Feb. 1975.

[7]Chen, C. H. S., "Prediction of Bead Area Contact Load at the Tire-Wheel Interface Using NASTRAN," *10th NASTRAN Users' Colloquium*, NASA Scientific and Technical Information Branch, NASA CP 2249, Washington, DC, 1982, pp. 133–142.

[8]*KYNAR Piezo Film Technical Manual*, Pennwalt Corp., Valley Forge, PA, 1987.

[9]Gross, T. S., Watt, D. W., Raber, R. S., Perault, J. A., and Zhang, Y., "Thermal Strain Response of Plated Holes," *Circuit World, Journal of the Institute of Circuit Technology*, Technical Journal of the Printed Circuit and Interconnection Federation, Vol. 18, No. 3, 1992, pp. 21–25.

[10]Raber, R. S., "Electro-Optic Interferometry with Noise Tolerant Phase Unwrapping," M.S. Thesis, Univ. of New Hampshire, Durham, NH, 1991.

[11]Huntley, J. M., "A Noise Immune Phase Unwrapping Algorithm," *Applied Optics*, Vol. 28, No. 16, 1989, pp. 3268–3270.

[12]"ADINA—A Finite Element Program for Automatic Dynamic Incremental Nonlinear Analysis," ADINA R&D, Inc., Rept. ARD 87-1, Watertown, MA, 1987.